

Failure mechanics of snow layers through image analysis

Original

Failure mechanics of snow layers through image analysis / De Biagi, V.; Barbero, Monica; Barpi, F.; Borri-Brunetto, M; Podolskiy, E.. - In: EUROPEAN JOURNAL OF MECHANICS. A, SOLIDS. - ISSN 0997-7538. - 74:(2019), pp. 26-33. [10.1016/j.euromechsol.2018.10.018]

Availability:

This version is available at: 11583/2715902 since: 2018-11-14T14:56:47Z

Publisher:

Elsevier

Published

DOI:10.1016/j.euromechsol.2018.10.018

Terms of use:

This article is made available under terms and conditions as specified in the corresponding bibliographic description in the repository

Publisher copyright

Elsevier postprint/Author's Accepted Manuscript

© 2019. This manuscript version is made available under the CC-BY-NC-ND 4.0 license
<http://creativecommons.org/licenses/by-nc-nd/4.0/>. The final authenticated version is available online at:
<http://dx.doi.org/10.1016/j.euromechsol.2018.10.018>

(Article begins on next page)

Failure mechanics of snow layers through image analysis

Valerio De Biagi^a, Monica Barbero^a, Fabrizio Barpi^a, Mauro Borri-Brunetto^a, Evgeny Podolskiy^b

^a*Department of Structural, Geotechnical and Building Engineering (DISEG) - Politecnico di Torino, C.so Duca degli Abruzzi 24, ITALY-10129 TORINO*

^b*Arctic Research Center – Hokkaido University, Kita-21 Nishi-11 Kita-ku, JAPAN-001-0021 SAPPORO*

Abstract

This paper is devoted to analyze the micro-mechanical behavior of snow layers subjected to shear force. A number of cold laboratory tests were performed on reconstructed snow samples on a specially designed direct shear apparatus and the loading process leading to the failure was recorded by a high-speed camera. The specimens were prepared under isothermal conditions and immediately tested in order to avoid sintering between the snow grains. Image analysis techniques (digital image correlation and particle image velocimetry) were applied on the camera records in order to obtain the snow strain history (during the loading phase) and the velocity field after the failure. Sequences of jamming and unjamming phases with the formation of vortices were observed. These observations confirm that snow layer failure process is similar to the one observed in other natural materials (e.g., sands). These results give an insight into triggering and failure propagation in a weak snow layer.

Keywords: Granular material; snow grains; PIV; DIC; shear failure; vortices

1. Introduction

The knowledge of the mechanical behavior of snowpack is a key requirement to understand snow avalanche triggering processes (Schweizer et al., 2003). Snowflakes are ice crystals that originate in the clouds and have complex shape and variable size depending on air temperature and excess vapor density on their surface. Snow falls on the ground and forms a complex porous medium (the snowpack) constituted of air, water vapor, ice and, sometimes, liquid water. Snowpack transforms with time, depending on the environmental conditions. Various types of metamorphisms can occur within the snowpack, varying its microstructure. When the temperature gradient is very low (isothermal metamorphism) and in absence of liquid water, a transfer of mass from the convex to the concave regions of the crystals occurs, inducing their progressive rounding and uniformity of their size, forming the so-called granular snow (snow with fine grains) (Flin et al., 2004). Such rounding leads to an increase in density, causing a snowpack to have a lower porosity and more contact areas between the crystals (McClung and Schaerer, 1993). Under such conditions, sintering between snow grains (i.e., grain bonding leading to improved strength) occurs because of the high homologous temperature of ice (Szabo and Schneebeli, 2007; Gubler, 1982).

The importance of snow microstructure for deformation processes has been known for many years. Experimental studies showed that the response of snow to applied loads is highly influenced by the bonding between snow grains, its breaking and rapid development (Shapiro et al., 1997).

Consideration of snow as a granular assembly has proved to be useful to understand how its micro-mechanical and optical properties affect macro-scale behavior (Nicot, 2004; Kaempfer et al., 2007). Recently, snow microstructure observations obtained by X-rays micro-tomography have being commonly used as an input to Discrete Element models (Johnson and Hopkins, 2005; Hagenmuller et al., 2014), or voxel-based Finite Element modeling (Srivastava et al., 2010). However, fracture tests studying weak layer micro-mechanical properties remain rare and difficult to conduct; especially, at fine time scales of fracture initiation corresponding to continuum-to-discrete transition. It appears that, in various natural materials (Tordesillas et al., 2016), stresses are transmitted through only a fraction of

Email address: valerio.debiagi@polito.it (Valerio De Biagi)

grains and these are grouped into chains. This process suggested an interesting similitude with the observations of the localization of deformation in granular materials. Recently, Barraclough et al. (2017) showed that deformation bands occur in initially homogeneous snow samples under homogeneous compaction load.

The localization of strain occurs in particular layers, called shear bands, of granular materials when subjected to shear. Inside the shear bands, vortex patterns of grains motion are observed. A simple shear stress field characterizes the deformation inside the shear band, i.e., a linear combination of pure shear deformation and rigid body rotation. The undefined slip field can be expressed as the sum of a uniform (affine) deformation field and a vortex (non affine deformation). Vortices mainly occur early in the load history, before the macroscopic sliding starts. They form inside the shear band: primary vortices are located in the center and rotate in the same direction than the shear band; secondary vortices, called wakes, rotate in the opposite direction and randomly grow next to the shear band boundaries mainly by drag from primary vortices. The grains outside the boundaries of the shear band move consistently with the shear direction. Experiments on granular artificial materials subjected to biaxial compression (Tordesillas, 2007) showed that failure occurred via strain localization. Vortices initially emerged throughout the sample, including near the boundaries, and then they progressively confined themselves to the persistent shear band. Vortices outside the band mainly emerged prior to shear banding, while in the failure regime they typically aligned along the central axis of the shear band between and besides two adjacent primary vortices. The governing mechanism of shear bands is the buckling of the force chain (Tordesillas et al., 2016). The force chain is defined as a set of particles within a compressed granular material that are held together and jammed into place by a network of natural compressive forces. The force chain is a sort of repository of stored energy accumulated at all the contacts along the chain prior to collapse, that occurs by buckling. During the failure process, three phases are recognized: (i) the jamming phase, in which stable force chains form, (ii) the late stages of jamming, in which force chains overload, resulting in buckling instability, and vortices form, and (iii) the unjamming period when the force chains collapse due to buckling. When buckling occurs, kinetic energy reaches peak values and is dissipated through friction. This process concentrates inside vortices, where grains undergo a motion that is a non affine deformation, which is significantly different from the affine one that characterizes the nearest neighbors grains. Force chain buckling is mainly confined inside or next to the boundaries of primary vortices. As much as certain force chains disappear because of their buckling, new force chains arise from extensions of an existing chain, typically close to shear band boundaries. After the unjamming phase, when the new generation of force chains is present, almost negligible kinematic activity is observed. Grains jam together and reach a new stable configuration. In this phase, no force chain buckling occurs and the vortex population, i.e., the number of vortices, drops. In the same manner as before, such new force chains will buckle and another stable configuration will be reached, and so forth. The jamming and unjamming events are associated to the transition from the solid-like (jamming, with the creation of force chains) to the fluid-like behavior (unjamming, in which contacts mobilize, starting from the relative motion at individual contacts via rolling and sliding) of granular materials.

Numerical (Williams and Rege, 1997; Kuhn, 1999) and experimental studies (Utter and Behringer, 2004) have been conducted on vortex structures and microbands in dense granular shear fields. In particular, such phenomena have been observed in geotechnical materials, such as sands. Rechenmacher (2006) applied digital image correlation technique (DIC) to measure two- and three-dimensional surface displacements on plane strain and axisymmetric sand specimens over short time steps, highlighting the role of the micro-deformation mechanisms responsible for the observed local strain non-uniformities that characterize the “steady-state” shear band evolution. Recently, Abedi et al. (2012) investigated the evolution of vortex structures within sands under shear strain. They found that the multiple-force chain collapse event induces the formation of co-rotating vortices and that local jamming at the conflux of opposing displacements between adjacent vortices arrests vortex motion. Thus, the critical state of deformation is micro-structurally characterized by a repeating temporal sequence of force chain collapse, vortex induction, jamming, vortex dissolution, and potential new force chain formation. The DIC experiments conducted on sands have shown that the shear band contains a narrower internal core of much higher strain (Viggiani, 2009). Moreover, Oda et al. (2004) identified columns of aligned grains in a shear band in a sand.

As stated, the observations made on the failure of snow specimen and the results related to the effects of sintering between snow grains appear similar to the phenomenon observed on dry granular materials, in particular on sands. In this paper, the authors intend to analyze in detail the failure of snow specimens made of snow grains with very low grain bonding in order to assess (i) if failure processes in snow layers can be somehow compared to those in dry sands, (ii) if rapid snow sintering affects the failure, and, more general, (iii) which experimental equipment is necessary and

which control parameters must be considered for studying shearing in snow layers.

Snow is a very delicate material: firstly, it is one of the most brittle geomaterials known to man (Kirchner et al., 2002); secondly, its manipulation is difficult because human heat can change its properties. When put into a testing machine, if the temperature of the machine is not perfectly equal to the one of the snow specimen, melting or freezing might occur, disturbing the specimen and invalidating the test. Because of that, in order to answer the previous issues, laboratory direct shear tests have been performed on snow samples in the controlled temperature conditions offered by a cold room. Considering snow as a frictional geomaterial, in a continuum mechanics approach, its strength can be described through two-parameters failure models, say Mohr-Coulomb criterion. On Mohr $\sigma - \tau$ plane, the criterion is represented by a couple of straight lines mathematically defined as

$$|\tau| = c + \sigma_n \tan \phi, \quad (1)$$

where τ and σ_n are the shear and normal stresses on the failure plane, respectively. The slope of the two lines, say ϕ , is the angle of internal friction, while c is the cohesion, i.e., the shear strength at zero normal stress. The failure surface can be expressed in terms of the stress invariants as

$$f(I_1, J_2, \theta) = -I_1 \sin \phi + \sqrt{J_2} \left[\frac{3(1 + \sin \phi) \sin \theta + \sqrt{3}(3 - \sin \phi) \cos \theta}{2} \right] - 3c \cos \phi = 0, \quad (2)$$

where I_1 is the first stress (hydrostatic) invariant and J_2 is the second deviatoric invariant. θ is the angle of similarity, or Lode angle (Chen and Saleeb, 2013). As expressed in Eqn.(2), the behavior of the material has to be investigated at different pressures p , since the criterion depends on the pressure p , i.e., $I_1 = 3p$. A shear stress field was induced on snow samples by a direct shear test apparatus especially conceived for snow tests; the failure process was recorded by a high speed camera for DIC and PIV analyses, as described in Section 2, in order to obtain the strain history and the velocity field induced into the snow during the test, respectively.

2. Methods

Camera-recorded direct-shear tests on reconstituted snow samples were performed in a cold laboratory (Centre d'Etudes de la Neige, St.-Martin-d'Hères, France, May, 2014) at a temperature of -10°C and a relative humidity $\approx 70\%$. A dedicated device able to apply a normal pressure and an increasing lateral force was used (Barbero et al., 2016).

2.1. Snow specimen preparation

Homogeneous cohesive snow slabs (density $\approx 360 \text{ kg m}^{-3}$ to 400 kg m^{-3}) were harvested in the French Alps (Col du Lautaret, 2000 m a.s.l.), transported by car in a refrigerated trailer, and stored in a cold storage room at -20°C . Faceted snow was created in the cold laboratory through temperature gradient metamorphism.

Each tested sample consisted of two square slabs of hard snow joined by a 10-mm-thick layer of sieved snow grains. Being our interest directed on the failure process inside the sieved snow layer, two shapes of the interface between hard slab and sieved snow were adopted to find which shape can guarantee the failure occurs inside the layer. One set of tests, identified as “flat”, were characterized by planar interface. The others, identified as “sawtooth”, had a profile with teeth with a period of 20 mm and 5 mm peak to peak amplitude. This solution was adopted following the suggestion of Nasuno et al. (1997) to transmit the shear force to the granular layer without interfacial slipping. Both profiles were created with specially constructed cutting tools.

Each sample was prepared in the following way.

1. Prismatic samples were cut from hard slabs, and used as lower and upper parts of snow “sandwiches” ($16 \text{ cm} \times 16 \text{ cm} \times 4 \text{ cm}$, and $16 \text{ cm} \times 16 \text{ cm} \times 3 \text{ cm}$, respectively). The appropriate cutting tool was used for profiling bottom and top hard slabs (Figure 1(a)). The snow characteristics of hard slabs are provided in Table 1.
2. The filling material was sieved onto the lower block and covered with the upper block after reprofiling (either flat or sawtooth), so that there was 10 mm of weak layer crystals (faceted snow) between the faces of the slabs (Figure 1(b)). The snow characteristics of the filling material are reported in Table 1.

Table 1: Snow characteristics of the different parts of the specimen. The snow type refers to the classification reported in Fierz et al. (2009). RGl: large rounded, usually elongated, and well sintered particles of size ≥ 0.25 mm; FC: faceted crystals; DH: depth hoar.

	Hard slab	Filling material
Density	$378 \pm 14 \text{ kg m}^{-3}$	$416 \pm 16 \text{ kg m}^{-3}$
Snow Type	RGl	FC/DH
Hand Hardness Index	Knife	Pencil
Shear Vane Resistance	$23.1 \pm 5.2 \text{ kPa}$	n.a.
Specific Surface Area	$21.2 \pm 1.71 \text{ m}^2 \text{ kg}^{-1}$	$14.8 \pm 1.23 \text{ m}^2 \text{ kg}^{-1}$
Optical Grain Diameter:	$0.3 \pm 0.03 \text{ mm}$	$0.4 \pm 0.03 \text{ mm}$

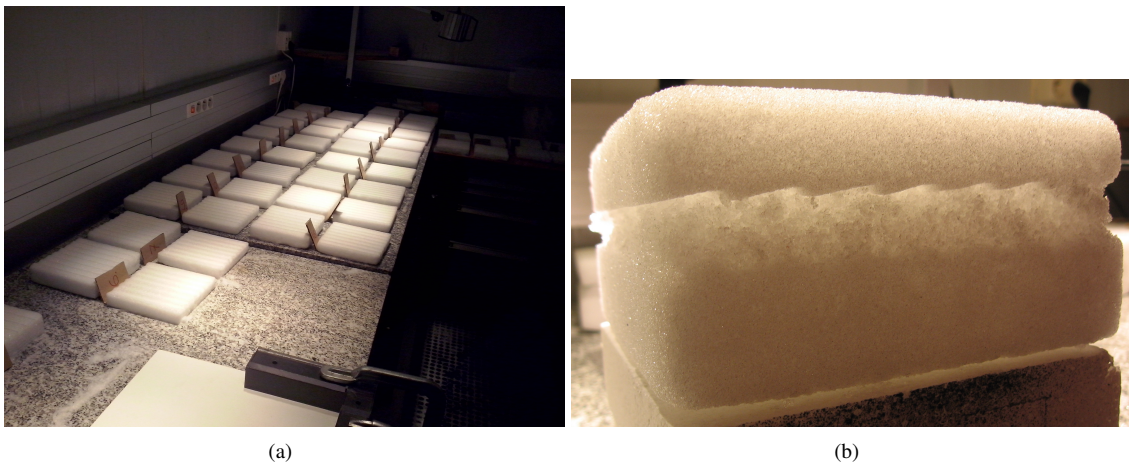


Figure 1: In (a): view of the laboratory with the cut and profiled hard slab halves prepared for being filled with the faceted snow simulating the weak layer. In (b): specimen with saw-tooth discontinuity, filled with sieved snow, ready to be tested.

2.2. The tests

The tests were performed with a direct shear test apparatus (Barbero et al., 2016; Podolskiy et al., 2014), modified in such a way that a rectangular window (5 cm×3 cm) at the side wall of the shear apparatus allowed to observe the displacement field in the upper and lower hard slabs and in the middle layer during shearing. The samples were tested immediately after the preparation.

During the test, a constant normal pressure was applied to the top of the sample by means of a pneumatic membrane. Three different vertical pressures were adopted: 0.5 kPa, 1.5 kPa and 3.0 kPa. A continuously increasing shear load was applied. The relative displacement between the moving parts of the shear apparatus, the shearing force as well as the vertical pressure were measured by a linear variable displacement transducer (LVDT), a load cell and a pressure gauge, respectively, and recorded by a NI CRio datalogger.

For documenting the fast process of failure, each test was filmed with a high-speed video camera (Baumer HXC1 with Nikon/Micro-NIKKOR-200-mm lens) operating at 500 fps (black and white, 1280 x 1024 pixels). The adopted lens are characterized by a very low geometric distortion, with a maximum value of 0.025% pincushion. Each frame was stored as a TIF image file. The camera was directed perpendicularly to the surface of interest, supported with continuous lights and located about 1.1 m away from the direct shear test apparatus. Its operation was controlled by a separate PC and camera time was stored in a metafile. It was not possible to trigger automatically both camera and testing apparatus because the systems were controlled by specific softwares. Working with very low cohesion material, maximum efforts were devoted to guarantee sufficient planarity of the observed snow surface. In this sense, the specimens were prepared using a mould, which was carefully removed in order to prevent accidental snow falling from the middle layer.

One of the major drawbacks observed during the preliminary tests is the lateral expulsion of ice grains after the failure. Because of that, it is not possible to follow the evolution of the vortices within the middle layer during the sliding because all the frames are affected by the falling snow. On the basis of previous experiences (Podolskiy et al., 2010; Reiweger et al., 2011; Reiweger and Schweizer, 2013), before testing, the exposed snow surfaces were sprayed with an ink in order to have good contrast for follow-up image analysis (it was found convenient to use black water-resistant paint allowing sharp, non-diffusive boundaries). Since the ink was manually sprayed, speckle pattern and quality vary from specimen to specimen. In general, the average size of the speckle is around 1 mm, even if, larger stains are present. The regions of interest identified during image analysis were accurately chosen not to include such undesired stains. A millimetre paper was attached on the drawer of the direct shear apparatus close to the surface of interest for the scaling of the camera records. After experiments on sawtooth profile visual inspection of specimens showed that the teeth remained intact and were never broken.

2.3. The elaboration of camera records

2.3.1. Synchronization of the records

The elaboration of camera records allows to highlight the failure mechanisms that might occur in the weak layer and to relate the observed effects on the specimen to the values of the measured variables. In order to achieve this objective, first, camera and NI CRio records were synchronized by comparing the displacements fields observed on the pictures and the ones measured through the LVDT. Metadata, i.e., temporal information related to each picture taken during the test, served for the synchronization. Particle image velocimetry (PIV) of both moving and fixed parts of the direct shear testing machine were analyzed. This allowed to monitor and to quantify the relative displacements between fixed and moving parts of the apparatus. The inertia of the moving components was a source of vibrations of the table onto which the testing equipment was lying; thus, the relative displacements between camera, fixed on a tripod, and apparatus were determined. The PIV were performed with PIVlab, a time-resolved digital particle image velocimetry tool for Matlab (Thielicke and Stamhuis, 2014). The software automatically compares the images and computes the velocity field of the selected regions of interest. The size of the region of interest (ROI) was about 240 x 240 pixels, corresponding to a real size of approximately 14 x 14 mm, Figure 2(a). The pixel to millimeters ratio was estimated measuring a reference length on the photographed millimeter paper. The temporal scale, i.e., the temporal distance between two frames, was set to 2 ms, being 500 Hz the frequency of the camera records.

Calling t the time in the temporal reference frame of the camera, the relative horizontal velocity, $u(t)$, i.e., the velocity between top and bottom part of the mechanical device, is determined by subtraction of the velocity fields found through the PIV, i.e.,

$$u(t) = u_t(t) - u_b(t), \quad (3)$$

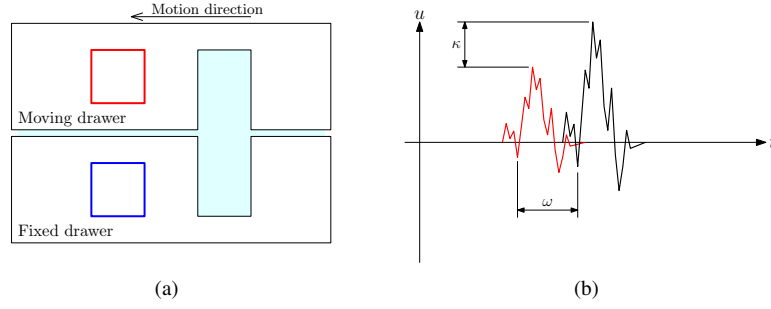


Figure 2: (a): regions of interest (ROI) of the PIV analysis for estimating the synchronization parameters of each test. The ROI of the fixed part and of the moving drawer of the direct shear apparatus are indicated with blue and red squares, respectively. (b): plot of the relative horizontal velocities u (in red) and u^* (in black), which is corrected in scale and time.

where $u_t(t)$ and $u_b(t)$ are the horizontal velocities averaged on each region of interest of the top and the bottom parts at time t . The u value was thus compared with the numerical time derivative, $v(\xi)$, of the real displacement that is measured by the linear variable displacement transducer (LVDT) installed on the apparatus. ξ is the value of time in the temporal reference frame of the records of the apparatus. The comparison was made by modifying the velocity u through two correction parameters, κ and ω . The former acted as a weighting factor on the scale, i.e., on the magnitude of the velocity; the latter served for shifting the values of the velocity on time axis, see Figure 2(b). In mathematical terms, a velocity function $u^* = u^*(u, t, \kappa, \omega)$ satisfying

$$u^*(t + \omega) = \kappa u(t) \quad (4)$$

was created. Adapted from Kolmogorov-Smirnov parametric test for comparing probability distributions (Smirnov, 1948), the values of the correction parameters are found by superimposing the plot of the corrected velocity u^* and the real velocity v and evaluating the maximum difference between the graphs at corresponding instants, i.e.,

$$\mathcal{F}(\kappa, \omega) = \max_{\xi} |v(\xi) - u^*(u, t, \kappa, \omega)|, \quad (5)$$

for a given pair of κ and ω . An unconstrained nonlinear minimization over the 2-parameters function $\mathcal{F}(\kappa, \omega)$ gives an estimate of κ and ω and allows to assign to each frame an instant in the temporal reference frame of the records of the apparatus. Then, the velocity fields of the top and the bottom halves of the mechanical device were determined through particle image velocimetry. The position of the regions of interest, i.e., the areas where the correlation analysis was made, are depicted in Figure 2(a). The displacement components of each of the two halves were determined by time integration of the corresponding velocity components.

2.3.2. Analysis before the failure

The unbroken specimen was considered as a continuous body and the distribution of the stresses and strains before failure at different levels of shear force was studied. The localization of strains in the weak layer and in top and bottom slabs was assessed through digital image correlation (DIC) techniques. A reduced set of frames was used; the outputs of the DIC are the three components of strain on the plane of the image. A Matlab open source package was used for the DIC (Jones et al., 2014). It allows to specify a region of interest of size 320 x 540 pixels and a grid along which the correlation is performed and displacements of points are evaluated. In order to define the appropriate grid size, a set of correlations adopting decreasing grid sizes were performed. The best grid had size 11x11 pixels (about 0.6x0.6 mm) and represents the minimum size allowing the possibility of performing the correlations at the instant of the failure. Finer grids would miss the strain field at the instant of failure since the displacement of corresponding points would be excessive. Displacements are smoothed prior to calculating strains. A Gaussian weight distribution alternatively centered at the control points, i.e., the centers of each 11x11 px cell, is adopted as smoothing function. The size of the distribution kernel is equal to 15 (Figure 3). The smoothing algorithm is repeated three times in order to provide robustness against the noise inherent to DIC. The infinitesimal strains were computed through an interpolation technique. As reported in Jones et al. (2014), a 16-nodes finite element is located in such a way that the

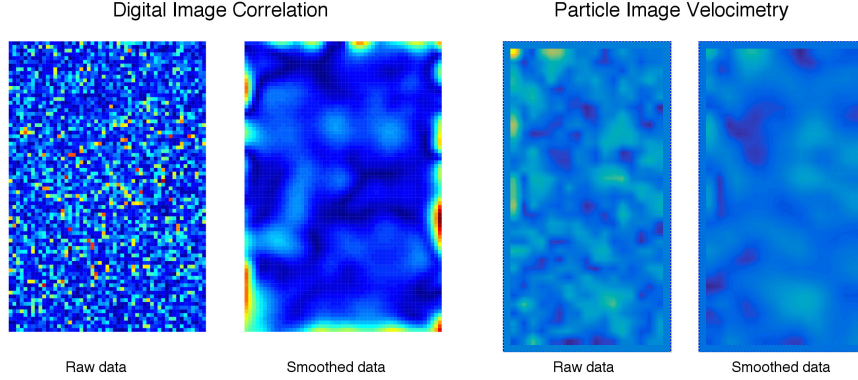


Figure 3: Raw data and smoothed data in DIC and PIV image analyses. The plot is related to two pictures related to non-deformed snow samples.

nodes of the finite element correspond to the control points. The element is mapped to a master element, interpolated and mapped back to the original element. The components of the small strain tensor are then calculated using the displacement derivatives computed at the nine Legendre-Gauss points of the master element.

We assume that the rupture occurs on xy plane, so that the out-of-plane strain is negligible. It is worthy to note that, in case of lack of planarity, large errors would affect the results (Sutton et al., 2009). This allows to classify the strain field as plane ($\varepsilon_z = 0$). In this framework, the output strains (ε_x , ε_y , γ_{xy}) of the DIC analysis were used for computing the first strain invariant J_1 , i.e.,

$$J_1 = \varepsilon_x + \varepsilon_y, \quad (6)$$

and von Mises strain invariant, i.e.,

$$\varepsilon_{vm} = \frac{2}{3} \sqrt{\varepsilon_x^2 + \varepsilon_y^2 - \varepsilon_x \varepsilon_y + \frac{3}{4} \gamma_{xy}^2}, \quad (7)$$

Both J_1 and ε_{vm} are invariant quantities, i.e., are independent of the orientation of the specimen with respect to the image frame, and, thus, are suitable for evaluating the effects of external loads in a continuum. The former reflects the local increase or decrease of volume and the latter the change in shape (distortion).

In order to estimate the noise from DIC calculations, the previously detailed procedure was applied to two pictures related to non-deformed snow samples, resulting in an average von Mises strain invariant equal to 0.1%. In addition, it is supposed that no relevant displacements orthogonal to the observation plane (out-of-plane) occur. This hypothesis, coupled with the fact that the observed surface has to be planar is one of the greatest limitations of the methodology.

2.3.3. Analysis after the failure

In this paper, we assumed that the failure occurs at the instant when the maximum force is measured. Following the failure, the behavior of the crystal grains composing the middle layer was studied through particle image velocimetry previously described.

The primary output of PIV technique is represented by a velocity field that, unfortunately, has a certain amount of noise, which induces significant errors when the velocity field is elaborated for getting further information (Nogueira et al., 1997). A preliminary post-processing data validation step was performed on the velocity field. In general, it was found that the majority of velocity vector moduli are bounded by well-defined values. The outliers are, thus, straightforwardly identified and manually removed. Among various possibilities for removing the additional noise (Garcia, 2010), a data smoothing technique was adopted. Following Raffel et al. (2013), a convolution of the data with a 3×3 kernel with equal weights was performed (Figure 3), as implemented in Thielicke and Stamhuis (2014).

From the resulting smoothed velocity field, the vorticity, i.e.,

$$\omega = \frac{\partial v}{\partial x} - \frac{\partial u}{\partial y}, \quad (8)$$

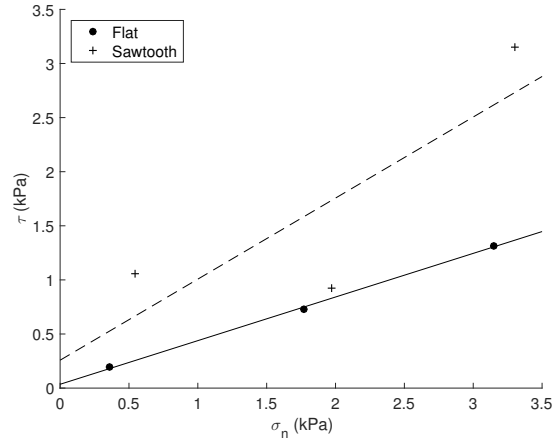


Figure 4: Mohr-Coulomb failure envelope on $\sigma_n - \tau$ Mohr plane.

where u and v are the horizontal and vertical components of the velocity vector, was computed. This parameter is often used to visualize vortices in flows: in the core of the vortex (rigid-body-like vortex) the magnitude of ω is larger than zero (anti-clockwise vortices have negative vorticity, clockwise vortices have positive vorticity), outside the vortex core (irrotational region) vorticity equals zero. Since vorticity is sensitive to shear (Stamhuis and Videler, 1995), visual analysis of the subsequent frames was conducted to confirm the presence of rotational structures within the middle layer. In the interpretation of the results, the Authors consider snow locally jammed when a conflux of opposing displacements between adjacent vortices, which arrest the vortices themselves, is observed. This is consistent with the definition by Abedi et al. (2012) which states that jamming occurs when the displacements are in opposition and relative motion is stalled. According to them, the regions in which affine-like deformations are observed are considered by the Authors as potential locations of force chains.

The post-failure analysis is limited to a very narrow time window. This is due to the fact that, as long as the two specimen halves move, ice grains are ejected. Thus, the results are compromised since the middle layer is not visible and there is a strong out-of-plane velocity component.

3. Results

The evolution of the strain state, the triggering of failure and the formation of multi-crystal rigid-body structures in flat and sawtooth specimens are herein described. As previously reported, three different normal pressures have been adopted for each set of tests. Plotting the results on Mohr plane, failure envelopes can be determined. Figure 4 shows the experimental results and the interpolating lines for the tests on flat and sawtooth samples. Adopting a classical geotechnical interpretation, the cohesion and the internal friction angle for flat tests are $c \approx 0$ kPa and $\phi = 22.0^\circ$, for the sawtooth tests $c = 0.26$ kPa and $\phi = 36.8^\circ$.

A summary of the results is reported in Tables 2 and 3. The failure force and the vertical pressure acting on the specimen are indicated in columns 2-3. In the following, the term “failure force” identifies the maximum force recorded during the test; “failure time” is the test time when the failure force was recorded. The figures in the fourth column display the von Mises equivalent strain at failure time. The colors indicate the parts that experience large distortions. Red areas are the ones in which the equivalent strain is large, blue areas the ones in which ε_{vm} is close to zero. The interface between top half-specimen and middle layer is marked with a dashed white line. The fourth column reports the location of the failure zone obtained through the DIC. Two cases are observed: the failure might occur either close to the interface or within the middle layer.

It can be observed that failure occurs in the portion of specimen where the large strains are recorded. In flat specimens (F1 to F3 in Table 2), failure occurs in the middle layer very close to the interface, independently of the value of the vertical pressure. In sawtooth specimens, failure occurs within the middle layer, far from the interface in test S1, characterized by the lowest value of normal stress, and close to the interface in tests S2 and S3.

Table 2: Tests on flat specimens. The load is applied right to left on the top part. The colormap of each figure serves for indicating the position of the maximum strains on the specimen, where the red color indicates the maximum von Mises equivalent strain. The size of each image is $36 \times 19 \text{ mm}^2$.

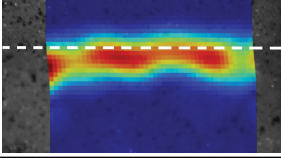
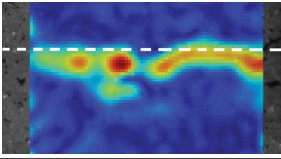
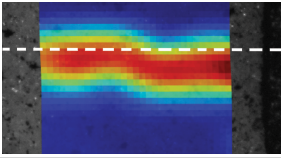
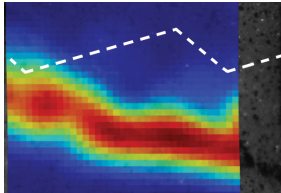
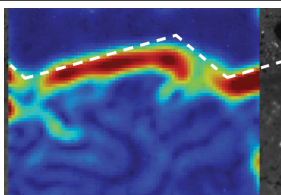
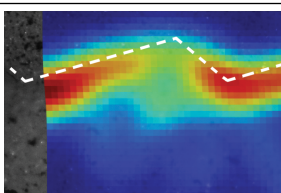
#	Failure force	Vertical pressure	ε_{vm} at failure	Location of failure
F1	5 N	0.36 kPa		Interface
F2	19 N	1.76 kPa		Interface
F3	34 N	3.15 kPa		Interface

Table 3: Tests on sawtooth specimens. The load is applied right to left on the top part. The colormap of each figure serves for indicating the position of the maximum strains on the specimen, where the red color indicates the maximum von Mises equivalent strain. The size of each image is $36 \times 24 \text{ mm}^2$.

#	Failure Force	Vertical pressure	ε_{vm} at failure	Location of failure
S1	27 N	0.55 kPa		Middle layer
S2	24 N	1.97 kPa		Interface
S3	81 N	3.31 kPa		Interface

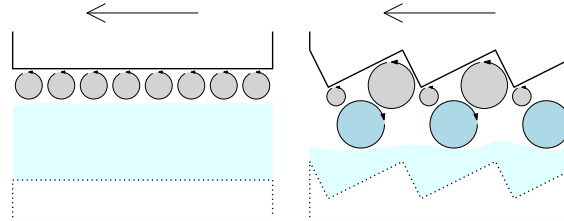


Figure 5: Sketch of the vortices observed in flat and sawtooth specimens after failure of the middle layer. The top halves moves leftwards; the counterclockwise and the clockwise vortices are depicted in grey and blue, respectively. Light-blue area represents the middle layer in which no rotating structures were observed.

The three different observed behaviors are analyzed in detail in the supplementary material, where a detailed description of the tests is reported. In detail, Section SM-1.1 illustrates the failure at the interface in flat specimens (reference to test F2), Section SM-1.2 the failure at the interface in sawtooth specimens (reference to test S2), Section SM-1.3 the failure within the middle layer in sawtooth specimen of test S1. The references to the figures contained in the supplementary material are marked with SM- prefix.

4. Discussion

Prior work has highlighted the granular nature of the snow constituting the snowpack and proved that the phenomena at the micro-scale have effects on the macro-scale behavior. For other natural granular-type materials, such as sands, it has been experimentally proved that the stresses are transmitted only by a fraction of grains through force chains. Shear tests on granular materials proved that the strain is localized within the shear bands, where material disturbance during the failure extends. The recent observations conducted by Barraclough et al. (2017) proved that strain localization occurs in snow samples subjected to compaction. The present research aims at observing the granular micro-phenomena that occurs in snow samples subjected to shear.

Referring to the shear strength of the tested specimens, various considerations can be drawn observing Fig. 4. The idea of adopting $\sigma-\tau$ axes for presenting the results comes from the classical approach for identifying failure envelope in natural materials. Considering that the test allowed to measure the peak strength, the interpretation of the results in Mohr plane by means of a linear interpolation seems to be contradictory since the filling material is the same for both flat and sawtooth tests. Different internal friction angles and cohesion among the testing configurations are found. In particular, as it is sketched in Figure 5, the shape of the interface between top and bottom halves affects the failure mode and, by consequence, the failure force. Different trends in the pre-failure phase are observed in the vertical displacement curves of tests S2 and F2. Although both tests show a local force peak before the maximum shear force is reached (see the red dots in Figs. SM-1 and SM-5), in test F2 no vertical displacement variation is recorded, while in test S2 a sudden drop of the upper half of the sample is observed. On the base of the above considerations, the Authors speculate that, for sawtooth specimen, the presence of inclined surfaces induces a lateral confinement with resulting higher lateral forces for triggering the shear rupture. This explain the fact that, on average, given a vertical pressure, the strength related to sawtooth specimens is higher than the one of flat specimens.

Referring to the first open question, related to the possibility of comparing the behavior of snow layers to the one of dry sands, despite our tests have been performed under load control, loosing the configuration at sliding, some structures very similar to those highlighted in sands (Abedi et al., 2012; Tordesillas, 2007; Tordesillas et al., 2016) are observed. All the structures are observed through an opening on the lateral side of the testing device. Despite that, the testing procedure (application of a uniform pressure on the whole area of the sample) and sample preparation technique allow to consider that the material in each layer is homogeneous and no differences between the edges and the centre of the sample are expected. All tests showed that, during the increase of the shear force, the deformation concentrates in some points inside the snow layer, usually close to the upper interface, as marked in red in the images included in Tables 2 and 3 and in Figures SM-2, SM-6 and SM-10. Then, the strain localization propagates forming a shear band close to the interface or crossing the middle layer (test S1). For higher values of vertical pressure, strain concentrations start in the first phase of shear loading (test F2). For lower values of vertical pressure, strain

concentrations start just before to the maximum shear load is reached (test S1). Excluding test S2, in the other cases a slight dilatancy is observed. It starts just prior to the failure force is reached and is more pronounced for lower values of applied vertical load. It seems that the normal confinement accelerates strain localizations and hinders the dilatancy. When strain localization starts, vortices and jamming zones appear. A sketch of such observed vortices is reported in Figure 5.

A sort of disturbance is observed from now on, characterized by a process of force chains collapse – formation of vortices – jamming – dissolution of vortices, similarly to what observed in sands. This phenomenon continues inside the shear band, also when failure occurs and during irreversible sliding. Due to loading control, only some instants in this last phase could be analyzed. For the same reason, a steady-state condition, which is simulated in Abedi et al. (2012), cannot be reached. In a tentative of interpreting test F2, which relates to flat specimen, a further PIV analysis was performed in the middle layer in order to investigate the presence of jamming and unjamming phases in the ice layer just prior to failure. The results of the investigation are reported in SM-1.1.3 This analysis, despite simple, highlights that the sequence force chain formation - force chain buckling - vortex formation also appears in the pre-peak phase. As noted before, due to the controlling test features, nothing can be assert on the presence of the observed phenomena in the steady state condition. Nevertheless, we expect that new tests on snow performed in strain controlled conditions will show the occurrence of jamming – unjamming cycles during the sliding into the shear band confirming the similarity of the behaviors of ice crystals and sand.

With reference to the second investigated point, a almost instantaneous sintering of the snow grains, observed during the preparation of the tested specimens (that is, the sieved snow stayed vertical when the preparation mould was removed) appears to affect the behavior of the specimen during the test. The DIC analysis performed during the loading phase shows that, as the shear load increases, the shear strains concentrate in the shear band until failure occurs, after which larger displacements are observed. Thus, no hardening occurs.

An interesting phenomenon related to the fact that the grains constituting the middle layer might have a very small, but not negligible, cohesion can be pointed out. As said, in the loading phase, strains (and thus stresses) are concentrated in certain areas of the middle layer, which deform and store elastic energy. The apparent cohesion (due to sintering and confinement) ensures the continuity of the medium, which can be treated as a continuum. For this reason, DIC technique is suitable for assessing the progression and the localization of the strains in the shear band. In addition, an elastic restitution phase is observed after the rupture. Despite the majority of the elastic energy stored in the specimen during the loading phase is released during the activation of the failure mechanism, a small part is restituted in elastic deformation. That is, as the upper part of the specimen monotonically moves towards left, just after the failure, the bottom part of the specimen moves rightwards.

5. Conclusions

Six direct shear tests on snow samples with artificial faceted snow layers in isothermal conditions have been presented in the paper, considering two surface profiles and three different vertical loadings. The horizontal force applied on the moving part of the direct shear testing apparatus, and its displacement, were measured with a load cell and a LVDT, respectively. The normal pressure acting on the specimen was measured by a pressure sensor. All the experiments were recorded with a high-speed camera (at 500 fps) manually triggered. First, the synchronization between instrument and camera frames was established by comparing the results of particle image velocimetry on the moving drawer and the displacements measured by the LVDT.

Due to the testing device limitations in terms of displacement control, two image analysis techniques were adopted in the two main phases of each experiment, i.e., pre- and post-failure. The evolution of the strain field within the snow sample before the failure was analyzed through digital image correlation technique. The post-failure behavior and the formation of vortices in the very first sliding phase within the soft middle layer was studied through particle image velocimetry. Despite the presence of camera records throughout all the duration of the test, the excessive lateral velocity caused broad differences between two subsequent frames in the post-failure phase, not adequate for performing pattern correlation, essential to perform DIC measurements. This problem can be overcome either by adopting displacement-controlled tests or, alternatively, by increasing the frame rate of the camera. A tentative of interpretation of the force chains in the pre-failure phase was proposed on Test F2, as illustrated in Figure SM-4.

As stated in the introduction, the main purpose of the paper is to understand shear failure mechanisms in natural granular materials, rather than setting a failure model for a snowpack. With this aim, the experimental campaign allowed to highlight the following evidences:

- the failure process of snow occurs by strain localization in a particular region defined as shear band. An appropriate mechanical modeling requires a mandatory analysis of grains kinematics since the deformation is no longer homogeneous and a bifurcation prior to failure occurs, with the evidence of vortices formation. This observation is fundamental in order to represent and model the mechanical behavior of snow. The presence of non-affine displacement field requires not to neglect the phenomena occurring at the grain scale, in such a way that the structure of the continuum model to be used to represent the snow mechanical behavior has to be modified in order to take into account the observed bifurcation phenomenon;
- the observations allow to state that the almost instantaneous sintering (coupled with the confinement) makes the snow specimen able to carry a shear load even at low normal forces. Furthermore, due to the fact that higher confinement pressures correspond to higher sintering rates (Podolskiy et al., 2014), this process accounts for the experimental observation that the shear band forms into the middle layer only in the case of sawtooth specimens with very low normal confinement. For reproducing zero-cohesion conditions it would be necessary to use depth hoar ice grains, i.e., snowflakes subjected to a metamorphism with high thermal gradients. Moreover, to assess the contribution of the confinement, all the normal forces must be removed, i.e., direct shear testing device could be installed vertically;
- it was observed that, in the majority of the cases, the failure process occurred close to the upper hard layer. This is probably due to the sample preparation procedure: the coarse snow is uniformly distributed onto the lower hard layer, then the upper hard layer is leaned onto the weak layer, inducing a sort of asymmetry into the system (the possible compressive stresses induced at the contact between the upper hard layer and the top of the weak layer are unknown). In addition to this factor, the presence of an almost instantaneous sintering in the coarse snow layer, could induce the failure process to occur close to the upper interface.

Referring to the needed experimental equipment and the choice of the control parameters for studying shearing in snow layers, a technique for investigating the failure mechanism of a layer of faceted snow grains has been proposed and discussed. The technique has interesting features: under special conditions, using non flat profiles like the sawtooth one suggested in the paper and applying low normal confinement, it is possible to induce a localization of shear strain within the middle layer. The failure should originate in this shear band. On the other hand, some drawbacks can be pointed out and solved in future experimental campaigns. Referring to the lateral expulsion of ice grains, one can overcome this problem by performing the test with the direct shear test device rotated of about 90 degrees. In this sense, the failure would occur on the vertical plane and the grains poured out from the middle layer would remain in place. This modification of the installation of the testing device would potentially ensure that the weight of the top half of the specimen does not affect the confinement force on the middle layer.

Future developments of the experimental device would require displacement control in the tests. Such requirement can be implemented in portable testing machines only through step-by-step motors. Pneumatic actuators require complicate pressure controls and feedback circuits for implementing a precise monotonically increasing displacement. Since a displacement-driven test would give more data on force-chain buckling, the other future challenges will focus on the influence of grain size, dimension and shape on the failure mechanism and the development of shear bands.

The results of the present (and future) studies significantly contribute to the knowledge and understanding of the mechanical behavior of snow in state of stress typical of various practical problems like the triggering of snow avalanches and stability of snowpacks on mountain slopes (land management, snow avalanche risk). This is the essential starting point to define an appropriate strength criterion and constitutive law for snow, to be used in modeling approaches.

Author's contributions All the authors participated to the experimental campaign and to the design of the tests; V. De Biagi and M. Barbero analyzed the images and interpreted the results.

Acknowledgements We thank R. Pallara (for the important help during the tests), J. Roulle (for cold room operation and collection of snow samples), G. Pulfer (for help with high-speed camera set-up), H. Bellot (for constructing continuous

light illumination), and P. Sprandre (for help with SSA measurements). The research leading to the experimental results was possible because of funding from the People Programme (Marie Curie Actions) of the European Union's Seventh Framework Programme (FP7/2007–2013) under REA grant agreement #298672 (FP7-PEOPLE-2011-IIF, “TRIME”) (E. Podolskiy). This work has also been supported by a grant from LabEx OSUG@2020 (Investissements d'avenir - ANR10 LABX56). Finally, the authors thank C. Scavia for the useful discussion on the interpretation of tests results, G. Chambon and M. Naaim for encouragement and support to pursue this experimental work.

References

- Abedi, S., Rechenmacher, A., Orlando, A., 2012. Vortex formation and dissolution in sheared sands. *Granular Matter* 14, 695–705.
- Barbero, M., Barpi, F., Borri-Brunetto, M., Pallara, O., 2016. An apparatus for in situ direct shear tests on snow. *Experimental Techniques* 40, 149–158.
- Barracough, T.W., Blackford, J.R., Liebenstein, S., Sandfeld, S., Stratford, T.J., Weinlander, G., Zaiser, M., 2017. Propagating compaction bands in confined compression of snow. *Nat Phys* 13, 272–275.
- Chen, W.F., Saleeb, A.F., 2013. Constitutive equations for engineering materials: Elasticity and modeling. volume 37. Elsevier.
- Fierz, C., Armstrong, R.L., Durand, Y., Etchevers, P., Greene, E., McClung, D.M., Nishimura, K., Satyawali, P.K., Sokratov, S.A., 2009. The international classification for seasonal snow on the ground. Technical Report. UNESCO/IHP Paris.
- Flin, F., Brzoska, J.B., Lesaffre, B., Coléou, C., Pieritz, R., 2004. Three-dimensional geometric measurements of snow microstructural evolution under isothermal conditions. *Annals of glaciology* 38, 39–44.
- Garcia, D., 2010. Robust smoothing of gridded data in one and higher dimensions with missing values. *Computational statistics & data analysis* 54, 1167–1178.
- Gubler, H., 1982. Strength of bonds between ice grains after short contact times. *Journal of Glaciology* 28, 457–473.
- Hagenmuller, P., Chambon, G., Flin, F., Morin, S., Naaim, M., 2014. Snow as a granular material: assessment of a new grain segmentation algorithm. *Granular Matter* 16, 421–432.
- Johnson, J.B., Hopkins, M.A., 2005. Identifying microstructural deformation mechanisms in snow using discrete-element modeling. *Journal of Glaciology* , 432–442.
- Jones, E., Silberstein, M., White, S.R., Sottos, N.R., 2014. In situ measurements of strains in composite battery electrodes during electrochemical cycling. *Experimental Mechanics* 54, 971–985.
- Kaempfer, T.U., Hopkins, M.A., Perovich, D.K., 2007. A three-dimensional microstructure-based photon-tracking model of radiative transfer in snow. *Journal of Geophysical Research: Atmospheres* 112, D24113.
- Kirchner, H., Michot, G., Schweizer, J., 2002. Fracture toughness of snow in shear and tension. *Scripta Materialia* 46, 425–429.
- Kuhn, M., 1999. Structured deformation in granular materials. *Mechanics of materials* 31, 407–429.
- McClung, D.M., Schaerer, P., 1993. *The Avalanche Handbook*. The Mountaineers, Seattle.
- Nasuno, S., Kudrolli, A., Gollub, J.P., 1997. Friction in granular layers: Hysteresis and precursors. *Physical Review Letters* 79, 949.
- Nicot, F., 2004. Constitutive modelling of snow as a cohesive-granular material. *Granular Matter* 6, 47–60.
- Nogueira, J., Lecuona, A., Rodriguez, P., 1997. Data validation, false vectors correction and derived magnitudes calculation on piv data. *Measurement Science and Technology* 8, 1493.
- Oda, M., Takemura, T., Takahashi, M., 2004. Microstructure in shear band observed by microfocus x-ray computed tomography. *Geotechnique* 54, 539–542.
- Podolskiy, E.A., Barbero, M., Barpi, F., Chambon, G., Borri-Brunetto, M., Pallara, O., Frigo, B., Chiaia, B., Naaim, M., 2014. Healing of snow surface-to-surface contacts by isothermal sintering. *The Cryosphere* 8, 1651–1659.
- Podolskiy, E.A., Nishimura, K., Abe, O., Chernous, P.A., 2010. Earthquake-induced snow avalanches: II. experimental study. *Journal of Glaciology* 56, 447–458.
- Raffel, M., Willert, C.E., Wereley, S., Kompenhans, J., 2013. *Particle image velocimetry: a practical guide*. Springer.
- Rechenmacher, A., 2006. Grain-scale processes governing shear band initiation and evolution in sands. *Journal of the Mechanics and Physics of Solids* 54, 22–45.
- Reiweger, I., Schweizer, J., 2013. Weak layer fracture: facets and depth hoar. *The Cryosphere* 7, 1447–1453.
- Reiweger, I., Simioni, S., Schweizer, J., 2011. Failure of weak snow layers. Ph.D. thesis. ETH.
- Schweizer, J., Jamieson, J.B., Schneebeli, M., 2003. Snow avalanche formation. *Reviews of Geophysics* 41, 1016.
- Shapiro, L.H., Johnson, J.B., Sturm, M., Blaisdell, G.L., 1997. *Snow mechanics: review of the state of knowledge and applications*. Technical Report. DTIC Document.
- Smirnov, N., 1948. Table for estimating the goodness of fit of empirical distributions. *The annals of mathematical statistics* 19, 279–281.
- Srivastava, P.K., Mahajan, P., Satyawali, P.K., Kumar, V., 2010. Observation of temperature gradient metamorphism in snow by x-ray computed microtomography: measurement of microstructure parameters and simulation of linear elastic properties. *Annals of Glaciology* 51, 73–82.
- Stamhuis, E., Videler, J., 1995. Quantitative flow analysis around aquatic animals using laser sheet particle image velocimetry. *Journal of Experimental Biology* 198, 283–294.
- Sutton, M., Ortu, J.J., Schreier, H., 2009. *Image correlation for shape, motion and deformation measurements*. Springer.
- Szabo, D., Schneebeli, M., 2007. Subsecond sintering of ice. *Applied Physics Letters* 90, 151916–151916.
- Thielicke, W., Stamhuis, E., 2014. Pivlab—towards user-friendly, affordable and accurate digital particle image velocimetry in matlab. *Journal of Open Research Software* 2, e30.
- Tordesillas, A., 2007. Force chain buckling, unjamming transitions and shear banding in dense granular assemblies. *Philosophical Magazine* 87, 4987–5016.

- Tordesillas, A., Pucilowski, S., Lin, Q., Peters, J., Behringer, R., 2016. Granular vortices: Identification, characterization and conditions for the localization of deformation. *Journal of the Mechanics and Physics of Solids* 90, 215–241.
- Utter, B., Behringer, R., 2004. Self-diffusion in dense granular shear flows. *Physical Review E* 69, 031308.
- Viggiani, G., 2009. Mechanisms of localized deformation in geomaterials: an experimental insight using full-field measurement techniques, in: *Mechanics of Natural Solids*. Springer, pp. 105–125.
- Williams, J., Rege, N., 1997. Coherent vortex structures in deforming granular materials. *Mechanics of Cohesive-frictional Materials* 2, 223–236.